

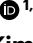

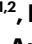
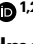

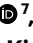



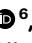



Flexoelectric polarizing and control of a ferromagnetic metal

Received: 2 May 2022

Accepted: 14 November 2023

Published online: 17 January 2024

 Check for updates

Wei Peng ^{1,2}✉, Se Young Park ³✉, Chang Jae Roh^{1,2,4}, Junsik Mun^{1,5}, Hwiin Ju⁴, Jinkwon Kim ^{1,2}, Eun Kyo Ko^{1,2}, Zhengguo Liang⁶, Sungsoo Hahn ^{1,2}, Jinfeng Zhang⁶, Ana M. Sanchez ⁷, David Walker ⁷, Steven Hindmarsh⁷, Liang Si ⁸, Yong Jin Jo⁹, Yongjoo Jo ¹⁰, Tae Heon Kim ⁹, Changyoung Kim^{1,2}, Lingfei Wang ⁶, Miyoung Kim^{1,5}, Jong Seok Lee ⁴, Tae Won Noh ^{1,2}✉ & Daesu Lee ^{10,11}✉

Electric polarization is well defined only in insulators not metals, and there is no general scheme to induce and control bulk polarity in metals. Here we circumvent this limitation by utilizing a pseudo-electric field generated by inhomogeneous lattice strain, namely a flexoelectric field, as a means of polarizing and controlling a metal. Using heteroepitaxy and atomic-scale imaging, we show that flexoelectric fields polarize the bulk of an otherwise centrosymmetric metal SrRuO₃, with off-centre displacements of Ru ions. This further impacts the electronic bands and lattice anisotropy of the flexo-polar SrRuO₃, potentially leading to an enhancement of electron correlation, ferromagnetism and its anisotropy. Beyond conventional electric fields, flexoelectric fields may be used to create and control electronic states through pure atomic displacements.

The polarization response of matter to an electric field forms an essential basis for many aspects of basic science and technology, such as ferroelectricity¹, piezoelectricity², magnetoelectricity³ and spintronics⁴. However, according to the modern theory of polarization, macroscopic electric polarization is well defined only in insulating crystals⁵. Gauss's law also states that the electrostatic field inside a metal is zero due to the screening by free charge carriers⁶. These have been fundamental challenges in understanding and manipulating bulk polarity in metals. Despite these limitations, the artificial control of bulk polarity in metals through an appropriate external field holds a great potential for scientific and technological endeavours, based on recently emerging quantum materials. For example, by modifying electronic band topology^{7,8} and real-space spin texture^{9,10}, the bulk polarity can be coupled

with conduction electrons, leading to novel electronic and spin-orbitronic functionalities. Exploring a general scheme for controlling the bulk polarity in metals is, thus, of great interest and demand.

To this end, we focus on flexoelectricity that describes the generation of electric polarization P_{flexo} in the presence of a strain gradient $\partial u/\partial z$ as $P_{\text{flexo}} = \epsilon f_{\text{eff}}(\partial u/\partial z)$, where ϵ is the dielectric constant, f_{eff} is the flexocoupling coefficient and u is the strain (Fig. 1a)^{11–15}. This effect is not limited to a certain crystal symmetry, so flexoelectricity is a universal property of all materials. Conceptually, flexoelectricity can be perceived as the polarization response of a medium to an applied flexoelectric field $E_{\text{flexo}} = f_{\text{eff}}(\partial u/\partial z)$. Importantly, E_{flexo} is not a real electric field that obeys Gauss's law but takes the essence of elastic fields. Thus, E_{flexo} should be regarded as a pseudo-electric field. It may be free

¹Center for Correlated Electron Systems, Institute for Basic Science, Seoul, Korea. ²Department of Physics and Astronomy, Seoul National University, Seoul, Korea. ³Department of Physics and Origin of Matter and Evolution of Galaxies (OMEG) Institute, Soongsil University, Seoul, Korea. ⁴Department of Physics and Photon Science, Gwangju Institute of Science and Technology, Gwangju, Korea. ⁵Department of Materials Science and Engineering and Research Institute of Advanced Materials, Seoul National University, Seoul, Korea. ⁶Hefei National Research Center for Physical Sciences at Microscale, University of Science and Technology of China, Hefei, China. ⁷Department of Physics, University of Warwick, Coventry, UK. ⁸Institut für Festkörperphysik, TU Wien, Vienna, Austria. ⁹Department of Physics and Energy Harvest-Storage Research Center (EHSRC), University of Ulsan, Ulsan, Korea. ¹⁰Department of Physics, Pohang University of Science and Technology, Pohang, Korea. ¹¹Asia Pacific Center for Theoretical Physics, Pohang, Korea. ✉e-mail: wei.peng@snu.ac.kr; sp2829@ssu.ac.kr; twnoh@snu.ac.kr; dlee1@postech.ac.kr

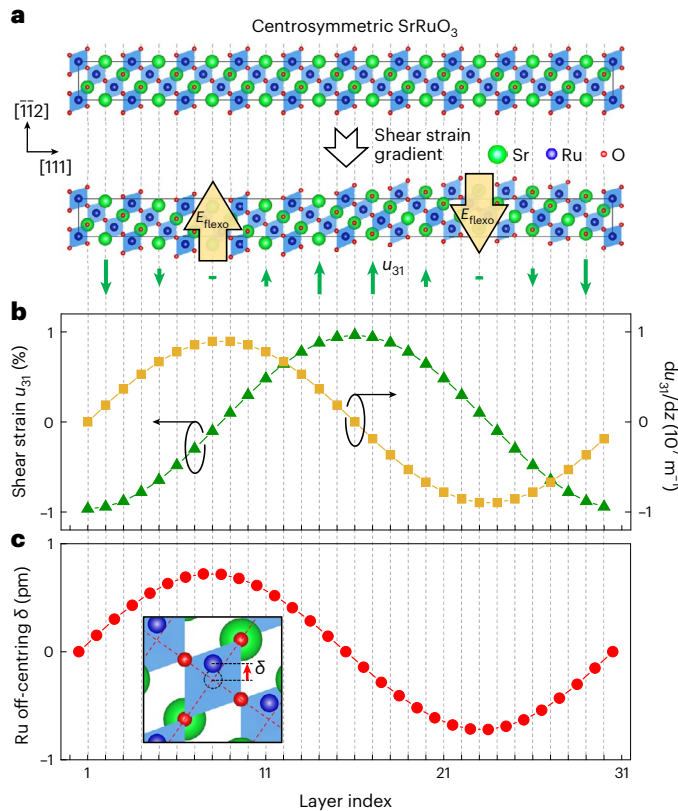


Fig. 1 | First-principles calculation of flexoelectricity of SrRuO₃. **a**, Schematics showing the flexoelectric field (E_{flexo}) generated from a gradient of shear strain (u_{31}) in perovskite oxides ABO₃. **b**, Plot of u_{31} (green triangles) and its gradient (du_{31}/dz ; yellow squares) in the theoretical SrRuO₃ supercell with u_{31} varying spatially by artificially imposing Sr shearing in a sinusoidal form. **c**, Calculated off-centre displacements of Ru atoms, extracted from the SrRuO₃ supercell under the shear strain gradient in **b**.

of electrostatic screening and could serve as a unique means for controlling the physical properties, including bulk polarity, of a metal¹⁶. However, despite recent theoretical predictions of a strong flexocoupling effect in metals^{17,18}, the existence of flexoelectricity in metals has yet to be experimentally validated. Here, we show theoretically and experimentally that E_{flexo} not only polarizes the bulk of a ferromagnetic metal SrRuO₃ but can also control its electronic properties.

Theoretical examination of flexoelectricity in a metal

We begin with a theoretical examination of the existence of flexoelectricity in SrRuO₃. We constructed a supercell of cubic SrRuO₃ in our theoretical simulation, as illustrated in Fig. 1a (see Methods for details). A sinusoidal shear strain u_{31} was imposed by artificially shearing Sr along the $[\bar{1}\bar{1}2]$ axis while relaxing the remaining ions (green triangles in Fig. 1b). Accordingly, a strain gradient was derived from $\partial u_{31}/\partial z$ (yellow squares in Fig. 1b). We found a sizable off-centre displacement of Ru, comparable to 1 pm under a strain gradient of $-9 \times 10^6 \text{ m}^{-1}$ (Fig. 1c). We further found that the ionic off-centring persists in SrRuO₃ regardless of the oxygen octahedral rotation (OOR) and the types of strain gradients, suggesting the robustness of flexoelectricity (Supplementary Figs. 1 and 2). Interestingly, a simulation of dielectric SrTiO₃ yielded similar off-centre displacements of cations (Supplementary Fig. 3). This finding is consistent with a recent theoretical work predicting comparable flexocoupling coefficients of a metal and a dielectric¹⁷. Moreover, we have thoroughly examined the polar instability of bulk SrRuO₃ in a variety of structures by zone-centre phonon calculations

(Supplementary Fig. 4). Theoretically, it seems that it is practically impossible to realize a polar structure in bulk ‘homogeneous’ SrRuO₃, in sharp contrast to the previously reported polar metals, for example LiOsO₃ and NdNiO₃ (refs. 19,20). This result thus emphasizes the critical role of strain gradients in polarizing SrRuO₃.

Experimental design of strain gradients in SrRuO₃

To achieve large strain gradients in SrRuO₃, we consider a heterostructure of SrRuO₃ epitaxially grown on a SrTiO₃ (111) substrate (Fig. 2a). In its bulk form, SrRuO₃ has a distorted, centrosymmetric perovskite structure with an OOR pattern described by $a^- a^- c^+$ according to Glazer notation (where a minus sign represents antiphase tilting and a plus sign represents in-phase tilting). It forms an orthorhombic structure ($Pbnm$) below 820 K. Our first-principles calculations predicted that, under moderate compressive (111)_{pc} strain (the subscript pc refers to pseudocubic; henceforth, the subscript pc will be omitted below), a monoclinic structure ($C2/c$) with an OOR pattern of $a^- a^- c^0$ and a rhombohedral structure ($R\bar{3}c$) with an OOR pattern of $a^- a^- a^-$ can be stabilized with small energy cost, compared to the orthorhombic structure (Supplementary Fig. 5). Further considering the strong interfacial structure coupling along the (111) orientation^{19,21}, we expect that the structure of the (111) SrRuO₃ evolves from rhombohedral at the interface to monoclinic within a certain thickness range (Supplementary Fig. 6). In line with the expected monoclinic and rhombohedral structures, the high-quality SrRuO₃ film on a SrTiO₃ (111) substrate (Supplementary Fig. 7) exhibits completely suppressed in-phase tilting (namely, the c^+ component) according to the half-integer Bragg diffraction (Supplementary Fig. 8).

Figure 2b schematically illustrates how to generate a large shear strain gradient, based on the inherent structural distortion in the (111) SrRuO₃. The main crystalline axis $[110]$ tilts away from the (111) plane, which is characterized by α . The theoretical value of α varies from 54.74° in cubic SrTiO₃ to 54.76° in rhombohedral SrRuO₃ and 56.14° in monoclinic SrRuO₃. When the SrRuO₃ layer is coherently bonded onto a cubic SrTiO₃ substrate, the competition between inherent structural distortion and the epitaxial coherence enforces a shear strain along the $[\bar{1}\bar{1}2]$ direction of the (111) plane. Accordingly, the shear strain u_{31} can be calculated as: $u_{31} = \Delta x/z = \cot \alpha_1 - \cot \alpha_2$, where Δx is the cation shearing distance along the $[\bar{1}\bar{1}2]$ direction and z is the (111) interplanar constant. α_1 is the expected tilt angle of SrRuO₃ that is presumed to be fully coherent with SrTiO₃, and α_2 is the actual tilt angle of low-symmetry distorted SrRuO₃. Therefore, as the interfacial SrRuO₃ is expected to adopt the rhombohedral structure, it should be subject to negligible shear strain as well as the associated gradient. Within a sufficient distance from the interface, the large α difference between monoclinic SrRuO₃ and cubic SrTiO₃ gives rise to a substantial shear strain of around 3.5%. Assuming structural relaxation within a thickness of 10 nm, a giant strain gradient of $3.5 \times 10^6 \text{ m}^{-1}$ can form, possibly polarizing SrRuO₃ through E_{flexo} .

Atomic-scale imaging of flexoelectricity in SrRuO₃

To directly visualize the expected, so-called flexo-polar SrRuO₃ at the atomic scale, we used scanning transmission electron microscopy (STEM) with the annular bright field (ABF) technique. Figure 2c clearly shows the shearing of Sr cations in SrRuO₃ away from the SrTiO₃ $[110]$ axis (red dotted line). By extracting the Sr positions along the $[110]$ atomic row (Supplementary Fig. 9), we evaluated the shear angle α and the shear strain. Although the shear strain is negligibly small in the interfacial region (~ 5 unit cells (u.c.)), it gradually develops to a maximum of -1.5% at the top, yielding an averaged shear strain gradient across the film as large as $2.5 \times 10^6 \text{ m}^{-1}$ along the $[\bar{1}\bar{1}2]$ direction. Then, such a large strain gradient causes the Ru ions in SrRuO₃ to be markedly displaced off-centre along $[\bar{1}\bar{1}0]$ (Fig. 2d,e), as they are subject to a vector component of the strain gradient. This is consistent with our calculation, which shows the lowest energy cost for the ionic displacement

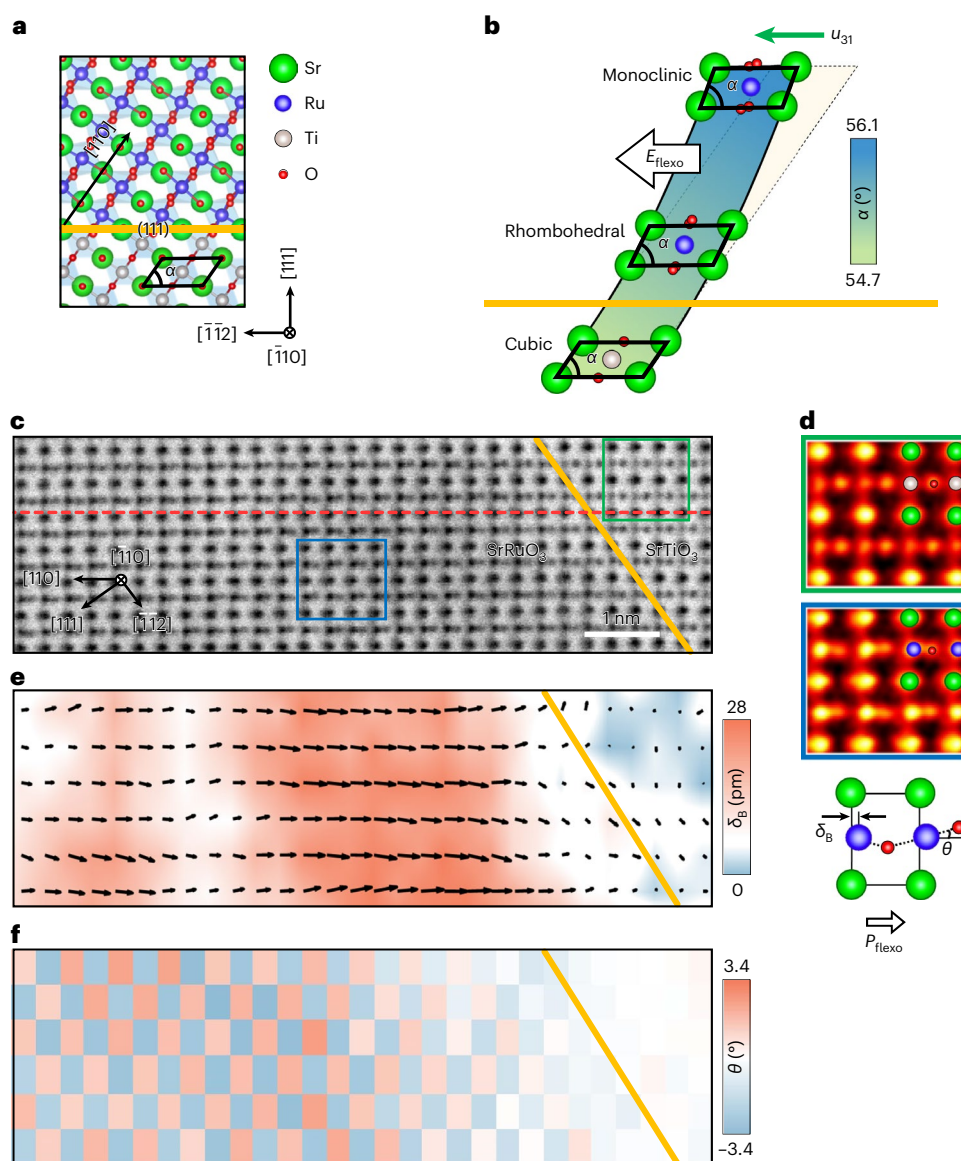


Fig. 2 | Atomic-scale imaging of the shear strain gradient and flexo-polar phase in SrRuO₃. **a**, Illustration of the SrRuO₃/SrTiO₃ (111) heterostructure with the cations aligned coherently. **b**, Schematic showing the formation of a shear strain and its gradient in the SrRuO₃/SrTiO₃ (111) heterostructure. **c**, Cross-sectional ABF-STEM image of the SrRuO₃/SrTiO₃ (111) heterostructure.

The red dashed line is drawn along the SrTiO₃ [110] direction for reference when visualizing the Sr shear in SrRuO₃. **d**, Zoomed-in images of representative SrTiO₃ and SrRuO₃ regions marked by the green and blue boxes in **c**, respectively. The bottom schematic shows the B-site cation displacement δ_B and the projected octahedral tilting angle θ . **e, f**, Mapping of δ_B (**e**) and θ (**f**) in **c**.

along [110] or $[\bar{1}\bar{1}0]$ (see Methods for details). The remarkable Ru displacement, greater than 25 pm locally (15 pm on average), is on par with that of the B-site cation in a prototypical ferroelectric oxide BaTiO₃. The large polarity from Ru off-centring is surprising since Ru ions dominantly contribute electrons at the Fermi level and should endure strong carrier screening of polar displacements. Therefore, the flexo-polar metal phase of SrRuO₃ is sharply distinct from the so-called Anderson–Blount polar metals such as LiOsO₃ and NdNiO₃ (ref. 19,20), whose polarity mainly comes from A-site cation displacements in a weak electron–phonon coupling scenario²².

Note that the experimentally observed Ru off-centring is a few tens of times larger than the theoretically predicted value under a comparable strain gradient in Fig. 1. To check if the discrepancy is from the choice of cell geometry for calculation and the form of strain gradients, we performed further calculations with a SrTiO₃/SrRuO₃/vacuum slab under a constant strain gradient to mimic the experimental

structure. Importantly, Ru off-centre displacements persist and are comparable to those under the sinusoidal strain gradients (Supplementary Discussion and Supplementary Fig. 10). Therefore, the underestimation of Ru off-centre displacements in our calculation should have other origins. For example, theoretical calculations are based on defect-free crystals without temperature effects, whereas the experimental measurements were conducted at room temperature and could have been strongly influenced by the amount of point defects and the electronic conductivity of the sample^{23,24}. In addition, huge strain gradients could cause a nonlinear flexoelectric response, leading to an order-of-magnitude enhancement of the flexoelectric effects in the experiments^{25,26}. Also note that, although our analysis of the STEM image focused on the shear strain gradient, a longitudinal strain gradient should naturally accompany the structural evolution along the out-of-plane direction, yielding additional E_{flexo} along $[\bar{1}\bar{1}\bar{1}]$ (Supplementary Fig. 1). This is a result of the different *c*-lattice constants of the

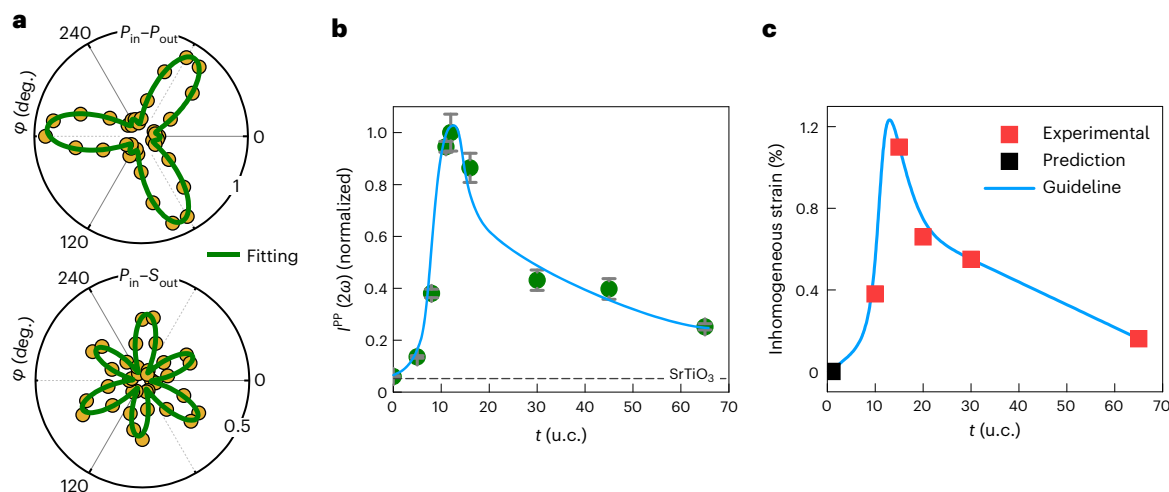


Fig. 3 | Correlation between strain gradient and polarity. **a**, SHG anisotropic patterns of a 12 u.c. $SrRuO_3/SrTiO_3$ (111) heterostructure acquired with the $P_{in}-P_{out}$ (upper) and $P_{in}-S_{out}$ (lower) configurations. Here, P and S stand for P - and S -polarised waves, respectively. The subscripts refer to incident (in) and outgoing (out) waves. **b**, SHG intensity $I^{PP}(2\omega)$ of (111) $SrRuO_3/SrTiO_3$ versus the $SrRuO_3$ film thickness, where $I^{PP}(2\omega)$ is the average intensity of the peaks in the SHG

pattern acquired in the $P_{in}-P_{out}$ configuration from two different samples for each thickness. The error bars represent the standard deviation. **c**, Inhomogeneous strain versus thickness from the W-H analysis (red squares) and the theoretically predicted values for the ultrathin film (≤ 5 u.c.; black square). The blue line is guidance for the eye.

monoclinic and rhombohedral structures calculated with the fixed in-plane lattice constants of the (111)-oriented $SrTiO_3$, which are 13.492 and 13.392 Å, respectively. This gives rise to a longitudinal strain of approximately 0.75%, corresponding to a strain gradient of $1.3 \times 10^6 \text{ m}^{-1}$, which is around half of the experimental value of the shear strain gradient. The longitudinal strain is not apparent in the STEM image, since the expected lattice variation is at most around -1 pm locally, which is below the detection limit of STEM. However, we suggest that E_{flexo} along $[\bar{1}\bar{1}\bar{1}]$ through longitudinal strain gradients, which should naturally exist, could cooperate with E_{flexo} along $[\bar{1}\bar{1}2]$ through shear strain gradients, thereby facilitating the actual Ru off-centring to align along the direction close to $[\bar{1}\bar{1}0]$ (Supplementary Fig. 2).

We further analysed the OOR of $SrRuO_3$ to examine its local structure change. As shown in Fig. 2d, the OOR manifests as a zigzag pattern of oxygen atoms and is characterized by the zigzag angle θ . In Fig. 2f, we map the θ of the same region by unit cell. Noticeably, both the OOR and the polarity are simultaneously suppressed in the interfacial $SrRuO_3$ region of -5 u.c. In addition, we found that the interfacial region shows a negligible strain gradient (Supplementary Fig. 11). These results are in line with the theoretically predicted rhombohedral $SrRuO_3$ at the interface and support the proposed scenario that the spatial evolution of the $SrRuO_3$ structure drives bulk flexo-polarity.

Correlation between strain gradient and Ru off-centring

To shed further light on the flexoelectric origin of the observed polar structure, we investigated the correlation between the polarity and strain gradient of the (111) $SrRuO_3$ film. We first used optical second-harmonic generation (SHG) to quantify the polarity of $SrRuO_3$. Figure 3a shows the threefold symmetric SHG anisotropy pattern of a $SrRuO_3/SrTiO_3$ (111) heterostructure, which is well fitted with the contribution of three electric dipoles in point group m (see Methods and Supplementary Fig. 6 for details). We plotted the SHG intensity $I^{PP}(2\omega)$ versus the thickness t in Fig. 3b. The plot exhibits a non-monotonic evolution, first increasing with thickness up to -13 u.c. and then gradually decreasing. This trend suggests that the measured SHG is dominantly contributed by the film bulk, consistent with the scenario of flexo-polarity. Therefore, these results confirm the emergence of a

polar monoclinic phase in the bulk of the $SrRuO_3$ film. Moreover, the 5 u.c. $SrRuO_3$ yielded rather distorted SHG patterns with considerably suppressed intensity (Supplementary Fig. 13), which is consistent with our STEM observation (Supplementary Fig. 12). This result again supports the proposed rhombohedral structure at the interface, which should lack a strain gradient and the associated flexo-polarity.

Then, we performed Williamson–Hall (W-H) analysis based on the X-ray diffraction (XRD) peak broadening of the $SrRuO_3$ film, which allowed us to estimate the inhomogeneous strain across the film²⁷. The analysis was done on films with a thickness of over 10 u.c., which yielded a sufficient XRD signal for a peak analysis (Supplementary Figs. 14 and 15). The extracted inhomogeneous strain versus the film thickness is plotted as red squares in Fig. 3c. To validate the results, we also extracted the coherence length along the out-of-plane direction from the W-H analysis, which exhibits a good correlation with the film thickness (Supplementary Fig. 15). Besides, the ultrathin films (≤ 5 u.c.) are predicted to possess negligible strain gradients (black square in Fig. 3c), which is also supported by our STEM measurement (Supplementary Fig. 12). Based on these results, the inhomogeneous strain in the (111) $SrRuO_3$ film evolves non-monotonically with the film thickness (the blue guideline in Fig. 3c). By simply assuming a linear strain profile, a similarly non-monotonic evolution of the strain gradient with the film thickness can be revealed (Supplementary Fig. 15). Comparing this result with the thickness-dependent SHG (Fig. 3b), we thus reveal a strong correlation between the strain gradient and the polarization.

Flexo-polar phase transition in $SrRuO_3$

As the monoclinic structural distortion plays a critical role in the flexo-polarity in $SrRuO_3$, conceivably, a polar-to-nonpolar phase transition would be coupled to a structural transition from the monoclinic to a higher-symmetry structure at high temperatures. The higher-symmetry structure is probably centrosymmetric rhombohedral according to the energy gain calculated for different structures. To investigate this, we measured the temperature-dependent SHG intensity of the (111) $SrRuO_3$ film (Fig. 4a). With increasing temperature, the polar-to-nonpolar transition seems to occur at -630 K, followed by a temperature-independent plateau of weaker intensity. The finite value of the latter part can be explained by the electric quadrupole

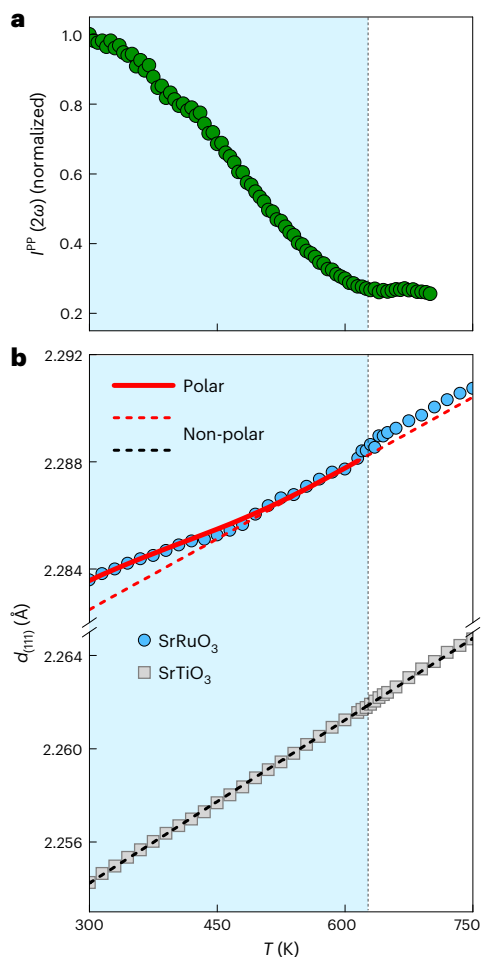


Fig. 4 | Flexo-polar phase transition in SrRuO₃. **a**, Temperature-dependent SHG intensity $I^{PP}(2\omega)$, obtained for the $P_{in}-P_{out}$ configuration. **b**, Temperature-dependent evolution of the (111) d spacing of SrRuO₃ (blue circles) and SrTiO₃ (grey squares). The uncertainty of the d spacing in our measurement (Methods) is approximately 3×10^{-5} and 1×10^{-6} Å for SrRuO₃ and SrTiO₃, respectively, but not shown here. The red solid line shows the predicted lattice evolution of the polar SrRuO₃. The red and black dashed lines show the lattice evolution, depending linearly on temperature, of nonpolar SrRuO₃ and SrTiO₃, respectively.

contribution of a centrosymmetric rhombohedral phase (Supplementary Fig. 16a). The transition can be described by a critical behaviour: $I^{PP}(2\omega) \propto (T_f - T)^\mu$, where the transition temperature T_f and the critical exponent μ are fitted as -630 K and 1.4, respectively (Supplementary Fig. 16b). The rather large μ is like those observed in improper ferroelectrics²⁸.

Furthermore, temperature-dependent XRD measurements confirm that the polar-to-nonpolar phase transition is coupled to a structural transition, as evidenced by a kink at ~630 K in the temperature-dependent (111) lattice constant of SrRuO₃ (Fig. 4b). The structural anomaly resembles the temperature-driven, symmetry-elevating structure transition observed in (001)-oriented SrRuO₃ films²⁹. The nonlinear evolution of the lattice constant below 630 K is a consequence of the electrostrictive-like expansion caused by Ru off-centring. The gradual evolution reflects the dependence of phase competition on temperature, for which the monoclinic and the rhombohedral phases are preferred below and above the structural transition temperature, respectively. Therefore, the energy landscape between the two phases is expected to be gradually flattened in the approach to the structural transition with increasing temperature,

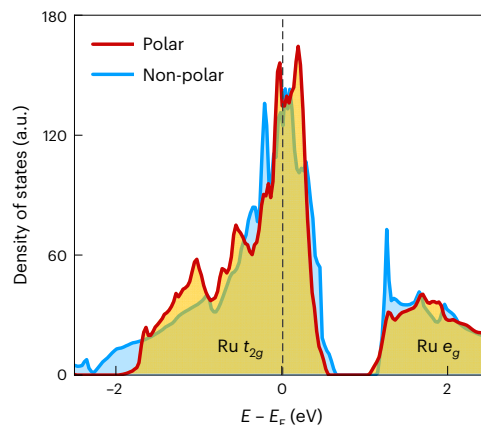


Fig. 5 | Flexoelectric control of the electronic band structure. Total density of states of the Ru d orbitals calculated for the nonpolar bulk SrRuO₃ (blue line) and the polar SrRuO₃ (red line) with a Ru off-centre displacement of 20 pm. a.u., arbitrary units.

resulting in metastable structures of intermediate distortion with less shearing and consequently less strain gradients. The evolution can be described by a thermodynamically derived equation:³⁰ $d_{(111)}(T) = d_{(111)}^{bulk}(T) \times [1 + aP(T)^2]$, as shown by the red solid line. In the equation, $d_{(111)}(T)$ and $d_{(111)}^{bulk}(T)$ are the lattice constants of the SrRuO₃ film and the nonpolar bulk SrRuO₃, respectively. $d_{(111)}^{bulk}(T)$ linearly depends on temperature due to thermal expansion (red dashed line). $P(T)$ is the polarity evolution of the SrRuO₃ film, which can be extracted from Fig. 4a. a is a constant related to elastic constants. We also verified the disappearance of the strain gradient above 630 K by temperature-dependent W-H analysis (Supplementary Fig. 17), which further corroborates the inferred flexo-polar phase transition.

Flexoelectric control of electronic properties in SrRuO₃

SrRuO₃ is a well-recognized correlated electron system that exhibits strong coupling among lattice, charge, spin and orbital degrees of freedom. Therefore, the markedly large Ru off-centre displacement is expected to profoundly impact the electronic properties of SrRuO₃, due to the change in the Ru–O bonding environment and the dominant contribution of Ru to electrons at the Fermi level. Indeed, our first-principles calculations show that Ru off-centring induces considerable reduction of the t_{2g} bandwidth (Fig. 5 and Supplementary Fig. 18), thereby enhancing electron correlation. This characteristic can be manifested in the reduced electron mobility, as suggested by our transport measurements (Supplementary Fig. 18 and Discussion). The enhanced electron correlation is also supposed to strengthen the magnetic ordering of SrRuO₃ according to Stoner theory (Supplementary Discussion)³¹, which can be supported by our magnetization measurements (Supplementary Fig. 19). Furthermore, we suggest that the uniaxial magnetic anisotropy of SrRuO₃ may be impacted by an inverse magnetostriction effect and the enhanced electron correlation originating from Ru off-centring (Supplementary Discussion and Supplementary Fig. 20). Although the detailed coupling mechanism between the electron/spin properties and Ru off-centring requires further extensive work, our results indicate the tremendous potential of flexoelectricity as a crucial tuning knob in metallic and magnetic materials.

Outlook

Bulk polarity tends to be incompatible with many technologically important electronic properties, such as metallicity, superconductivity, ferromagnetism and strong spin–orbit coupling. Challenging

this, our study reveals that bulk flexo-polarity in a metallic ferromagnet SrRuO₃ could even enhance ferromagnetism while preserving the metallicity with little loss. Given the universality of flexoelectricity¹¹, our approach is generally applicable to a wide range of materials. Note that although our analysis has focused on the gradients of shear and longitudinal strain originating from the thickness-dependent structural transition, other sources of strain gradients may also contribute and require further microscopic structure characterization for clarification, for example, the ferroelastic domain walls (Supplementary Fig. 6). Moreover, an important question left for future theoretical and experimental research is the actual flexoelectric coefficients of metals. Importantly, experimental methods for applying flexoelectric fields have recently been well established³², with several outstanding characteristics, including universality, non-destructiveness and high speed. Thus, these recent advances in experimental techniques further improve the prospects for exploring exotic physical properties using flexoelectric fields.

Online content

Any methods, additional references, Nature Portfolio reporting summaries, source data, extended data, supplementary information, acknowledgements, peer review information; details of author contributions and competing interests; and statements of data and code availability are available at <https://doi.org/10.1038/s41567-023-02333-8>.

References

1. Scott, J. F. Applications of modern ferroelectrics. *Science* **315**, 954–959 (2007).
2. Fu, H. & Cohen, R. E. Polarization rotation mechanism for ultrahigh electromechanical response in single-crystal piezoelectrics. *Nature* **403**, 281–283 (2000).
3. Garcia, V. et al. Ferroelectric control of spin polarization. *Science* **327**, 1106–1110 (2010).
4. Trier, F. et al. Oxide spin–orbitronics: spin-charge interconversion and topological spin textures. *Nat. Rev. Mater.* **7**, 258–274 (2022).
5. Resta, R. Macroscopic polarization in crystalline dielectrics: the geometric phase approach. *Rev. Mod. Phys.* **66**, 899–915 (1994).
6. Jackson, J. D. *Classical Electrodynamics* (Wiley, 1998).
7. Zhang, C.-L., Liang, T., Bahramy, M. S. & Tokura, Y. Berry curvature generation detected by Nernst responses in ferroelectric Weyl semimetal. *Proc. Natl Acad. Sci.* **118**, e2111855118 (2021).
8. Xiao, J. et al. Berry curvature memory through electrically driven stacking transitions. *Nat. Phys.* **16**, 1028–1034 (2020).
9. Wang, L. et al. Ferroelectrically tunable magnetic skyrmions in ultrathin oxide heterostructures. *Nat. Mater.* **17**, 1087–1094 (2018).
10. Sokolov, D. A. et al. Metamagnetic texture in a polar antiferromagnet. *Nat. Phys.* **15**, 671–677 (2019).
11. Zubko, P., Catalan, G. & Tagantsev, A. K. Flexoelectric effect in solids. *Annu. Rev. Mater. Res.* **43**, 387–421 (2013).
12. Lee, D. et al. Giant flexoelectric effect in ferroelectric epitaxial thin films. *Phys. Rev. Lett.* **107**, 057602 (2011).
13. Catalan, G. et al. Flexoelectric rotation of polarization in ferroelectric thin films. *Nat. Mater.* **10**, 963–967 (2011).
14. Lu, H. et al. Mechanical writing of ferroelectric polarization. *Science* **336**, 59–61 (2012).
15. Yang, M. M., Kim, D. J. & Alexe, M. Flexo-photovoltaic effect. *Science* **360**, 904–907 (2018).
16. Lipatov, A. et al. Direct observation of ferroelectricity in two-dimensional MoS₂. *npj 2D Mater. Appl.* **6**, 18 (2022).
17. Zabalo, A. & Stengel, M. Switching a polar metal via strain gradients. *Phys. Rev. Lett.* **126**, 127601 (2020).
18. Yurkov, A. S. & Yudin, P. V. Flexoelectricity in metals. *J. Appl. Phys.* **129**, 195108 (2021).
19. Kim, T. H. et al. Polar metals by geometric design. *Nature* **533**, 68 (2016).
20. Shi, Y. et al. A ferroelectric-like structural transition in a metal. *Nat. Mater.* **12**, 1024–1027 (2013).
21. Kim, J. R. et al. Stabilizing hidden room-temperature ferroelectricity via a metastable atomic distortion pattern. *Nat. Commun.* **11**, 4944 (2020).
22. Puggioni, D. & Rondinelli, J. M. Designing a robustly metallic noncentrosymmetric ruthenate oxide with large thermopower anisotropy. *Nat. Commun.* **5**, 3432 (2014).
23. Hong, J. & Vanderbilt, D. First-principles theory and calculation of flexoelectricity. *Phys. Rev. B* **88**, 174107 (2013).
24. Wang, L. et al. Flexoelectronics of centrosymmetric semiconductors. *Nat. Nanotechnol.* **15**, 661 (2020).
25. Harbola, V. et al. Strain gradient elasticity in SrTiO₃ membranes: bending versus stretching. *Nano Lett.* **21**, 2470 (2021).
26. Das, S. et al. Enhanced flexoelectricity at reduced dimensions revealed mechanically tunable quantum tunneling. *Nat. Commun.* **10**, 537 (2019).
27. Catalan, G. et al. Strain gradients in epitaxial ferroelectrics. *Phys. Rev. B* **72**, 020102 (2005).
28. Bousquet, E. et al. Improper ferroelectricity in perovskite oxide artificial superlattices. *Nature* **452**, 732–736 (2008).
29. Choi, K. J. et al. Phase-transition temperatures of strained single-crystal SrRuO₃ thin films. *Adv. Mater.* **22**, 759–762 (2010).
30. Zembilgotov, A. G., Pertsev, N. A., Kohlstedt, H. & Waser, R. Ultrathin epitaxial ferroelectric films grown on compressive substrates: competition between the surface and strain effects. *J. Appl. Phys.* **91**, 2247–2254 (2002).
31. Wahle, J., Blümer, N., Schlipf, J., Held, K. & Vollhardt, D. Microscopic conditions favoring itinerant ferromagnetism. *Phys. Rev. B* **58**, 12749–12757 (1998).
32. Park, S. M. et al. Flexoelectric control of physical properties by atomic force microscopy. *Appl. Phys. Rev.* **8**, 041327 (2021).

Publisher's note Springer Nature remains neutral with regard to jurisdictional claims in published maps and institutional affiliations.

Open Access This article is licensed under a Creative Commons Attribution 4.0 International License, which permits use, sharing, adaptation, distribution and reproduction in any medium or format, as long as you give appropriate credit to the original author(s) and the source, provide a link to the Creative Commons license, and indicate if changes were made. The images or other third party material in this article are included in the article's Creative Commons license, unless indicated otherwise in a credit line to the material. If material is not included in the article's Creative Commons license and your intended use is not permitted by statutory regulation or exceeds the permitted use, you will need to obtain permission directly from the copyright holder. To view a copy of this license, visit <http://creativecommons.org/licenses/by/4.0/>.

© The Author(s) 2024

Methods

Theoretical calculation

First-principles density functional theory (DFT) calculations were performed within the local density approximation plus U (LDA + U) scheme using the Vienna ab initio simulation package (VASP, ref. 33). The projector augmented-wave method was used with the Ceperley–Alder exchange–correlation functional³⁴. The on-site Coulomb interaction considered by rotationally invariant LDA + U was parameterized by $U = 3$ eV and $J = 0.75$ eV for Ru d orbitals³⁵. The choice of the parameters was consistent with that in other studies^{36,37}. We used the charge-only LDA exchange–correlation functional with the plus U extension, giving increasing exchange splitting proportional to J for SrRuO₃ (ref. 38). With our choice of the exchange–correlation functional and parameters for on-site Coulomb interaction, the calculated lattice constants and magnetic moments of the bulk SrRuO₃ in $Pbnm$ space group are in good agreement with experimental data (Supplementary Table 3 and Supplementary Fig. 21). Moreover, the calculated magnetic moment of a (111)-oriented $Imma$ structure relaxed with fixed hexagonal in-plane lattice constants of SrTiO₃ was $2\mu_B/\text{Ru}$ with a moderate overestimation relative to the experimental value of $1.58\mu_B/\text{Ru}$ (Supplementary Fig. 19). The increase in the magnetic moment may be due to the static mean-field approximation of DFT, as the DFT plus dynamical mean-field theory study of SrRuO₃ (ref. 39) shows a decreased magnetic moment of $1.6\mu_B/\text{Ru}$. We used an energy cutoff of 500 eV. The k -point samplings of $6 \times 6 \times 4$ for the 20-atom $\sqrt{2} \times \sqrt{2} \times 2$ unit cell, $6 \times 6 \times 3$ for the 30-atom $\sqrt{2} \times \sqrt{2} \times 2\sqrt{3}$ unit cell and $3 \times 3 \times 3$ for the 120-atom $2\sqrt{2} \times 2\sqrt{2} \times 2\sqrt{3}$ unit cells were used for bulk and strained-bulk calculations. To evaluate the flexoelectric distortions, we used $6 \times 6 \times 1$ k -point samplings for the 150-atom $\sqrt{2} \times \sqrt{2} \times 10\sqrt{3}$ (111)-oriented supercells and also for the 120-atom (111)-oriented vacuum/slab geometries. For the slab calculations, the dipole correction implemented in VASP was used. The atomic positions were relaxed with a force threshold of 0.02 eV/Å.

The flexoelectric distortions were calculated for two different supercell orientations. For the strain gradient in the [111] direction, two $\sqrt{2} \times \sqrt{2} \times 10\sqrt{3}$ hexagonal supercells were constructed based on the fully relaxed five-atom cubic SrRuO₃ (space group $Pm\bar{3}m$) and 20-atom orthorhombic SrRuO₃ (space group $Imma$) structures with $a^0 a^0 a^0$ and $a^- a^- c^0$ Glazer symbols, respectively. We found no ferroelectric instability in the cubic and orthorhombic structures. The initial atomic structure of each supercell was prepared with the shear and/or longitudinal displacement of the i th atom with an amount of $h \times Nc \sin\left(\frac{2\pi n z_i}{Nc}\right)$, where N is the number of unit cells in the z direction, c is the hexagonal out-of-plane bulk lattice constant, z_i is the position along the direction of the strain gradient and h is a parameter controlling the strain gradient⁴⁰. The parameter h was set to produce a maximum shear strain gradient of $9 \times 10^6 \text{ m}^{-1}$, comparable to the experimental value ($3.5 \times 10^6 \text{ m}^{-1}$). A maximum longitudinal strain gradient of $4.5 \times 10^6 \text{ m}^{-1}$ was applied, based on the change in the out-of-plane lattice constant of 0.75% between rhombohedral and monoclinic structures in strained-bulk calculations (Supplementary Table 2), corresponding to approximately half of the shear strain gradient. When fixing the Sr atoms at the initial positions, the atomic positions of the Ru and O atoms were relaxed. The off-centre displacements of Ru atoms from the initial positions were measured. The flexoelectric distortion of SrTiO₃ was calculated in the same way for a (111)-oriented supercell, constructed based on the relaxed cubic structure.

To investigate the preferred direction of Ru off-centring, we calculated the energy cost of shifting the Ru atoms by 0.05 Å along different pseudocubic directions: [100], [010], [001], [110], [101], [011], [111] and $[\bar{1}\bar{1}\bar{1}]$. The calculated energy cost per formula unit for these directions relative to the [110] direction is 0.61, 0.61, 2.46, 0, 1.37, 1.37, 0.71 and 1.29 meV, respectively.

The change in the partial density of states as a function of Ru displacement was evaluated by gradually shifting the Ru positions along

the pseudocubic $[\bar{1}\bar{1}\bar{0}]$ direction from those in the relaxed $Imma$ ($a^- a^- c^0$) structure. We calculated the nonmagnetic partial density of states of Ru d orbitals, which dominantly contribute the electronic states at the Fermi level and are mainly responsible for the electronic properties of SrRuO₃.

Sample fabrication and characterization

SrRuO₃ films were grown on (001) or (111) SrTiO₃ substrates using a pulsed-laser deposition system with a KrF excimer laser (248 nm). A high-pressure reflection high-energy electron diffraction system was used to monitor the growth. Before deposition, SrTiO₃ substrates (miscut <0.1°) were etched with a buffered hydrofluoric acid solution and then annealed in air at 1,050 °C for 1 h to produce an atomically flat surface with a unit-cell step terrace structure. The substrates obtained were further leached in deionized water for 1 h to remove excess Sr on the surface. During deposition, the temperature of the substrate was maintained at 675 °C. Ultrathin SrRuO₃ films were grown under an oxygen pressure of 100 mTorr with a laser fluence of 2 J cm⁻².

Atomic force microscopy was performed using a Cypher scanning probe microscope (MFP-3D, Asylum Research) with Ir-Pt-coated tips (PPP-EFM, Nanosensors). A room-temperature θ - 2θ scan and reciprocal space mapping by XRD were performed with a Bruker D8 Discover. Half-integer Bragg diffraction and temperature-dependent ω - 2θ scans were carried out using synchrotron XRD at the 3A beamline of Pohang Accelerator Laboratory. The (111) lattice constants of SrRuO₃ and SrTiO₃ were extracted from a Gaussian fitting of the (222) peaks with uncertainty. For the temperature-dependent W-H analysis, we used a high-resolution XRD (Panalytical X'pert Pro MRD) equipped with a four-bounce Ge 220 cut monochromator giving pure Cu $K\alpha_1$ radiation and an Anton Paar DHS 1100 domed hot stage. The sample was aligned at each temperature to account for the thermal expansion of the stage. We used a Pearson VII function to fit the XRD peaks:

$$I(2\theta) = I_{\max} \frac{w^{2m-1}}{[w^2 + 4(2^{1/m} - 1)(2\theta - 2\theta_0)^2]^m}$$

This function becomes a Lorentzian as $m \rightarrow 1$ and a Gaussian as $m \rightarrow \infty$. As we mostly fitted the XRD data with $m > 50$, our fits reasonably correspond to Gaussian fits. W-H analysis uses a quadratic relation, that is, $(\beta \cos \theta)^2 = (K \frac{\lambda}{D})^2 + (4u_i \sin \theta)^2$, for Gaussian peaks and a linear relation, that is, $\beta \cos \theta = K \frac{\lambda}{D} + 4u_i \sin \theta$, for the Lorentzian, where D is the coherence length, λ is the X-ray wavelength and K is a geometrical constant close to 1 (usually 0.9). Therefore, we performed the W-H analysis using the quadratic relation. From the slope of linear fits of $(\beta \cos \theta)^2$ versus $(4 \sin \theta)^2$, we estimated the inhomogeneous strain u_i . Also, from the intercept at the origin of linear fits of $(\beta \cos \theta)^2$ versus $(4 \sin \theta)^2$, we estimated the coherence length D .

SHG measurement

SHG measurements were performed with two femtosecond wave sources possessing central wavelengths of 800 and 840 nm and repetition rates of 80 MHz and 250 kHz, respectively. The polarization of the fundamental wave and the second-harmonic wave was controlled by a half-wave plate and a Glan–Taylor polarizer, respectively. We isolated the SHG wave from the fundamental wave by adopting low-pass and band-pass filters, and the isolated SHG wave was detected by a photomultiplier tube. The laser fluence for the SHG measurement was 0.127 mJ cm⁻², which did not induce any visible damage during the experiment. We found that surface burning occurred once the laser fluence was increased to several mJ cm⁻² with continuous illumination for 30 min. Temperature-dependent measurements were carried out in an incident-plane-rotating set-up with a high-temperature stage (HCP621G; Instec; ref. 41).

The SHG results were analysed with both electric quadrupole (EQ) and electric dipole (ED) contributions, which are given by

$I_{\text{EQ}}^{\omega} \propto |E_{\text{EQ}}^{2\omega}|^2 = |\chi_{ijkl} E_j^{\omega} \partial_k E_l^{\omega}|^2$ and $I_{\text{ED}}^{2\omega} \propto |E_{\text{ED}}^{2\omega}|^2 = |\chi_{ijk} E_j^{\omega} E_k^{\omega}|^2$, respectively. Here, E_i^{ω} denotes the electric field component of the fundamental wave with optical polarization along the i axis. χ_{ijkl} and χ_{ijk} represent the second- and third-order susceptibility tensor components, respectively. For the room-temperature polar phase of SrRuO₃, we used the electric dipole contribution of three equivalent polar monoclinic domains with point group m for fitting in consideration of the observed polar axis. For the high-temperature nonpolar phase, we considered the electric quadrupole contribution of a nonpolar rhombohedral structure with point group $\bar{3}m$ for fitting. In the following, we provide the nonlinear susceptibility tensor components allowed for the considered crystal symmetry and the details of the analysis.

For the electric dipole contribution of three equivalent polar monoclinic domains (point group m ; Supplementary Fig. 6), the second-order susceptibility tensors for the monoclinic point group m are

$$\chi_{xxx}, \chi_{xyy}, \chi_{xzz}, \chi_{zxx}, \chi_{xxz}, \chi_{yyz}, \chi_{zyz},$$

$$\chi_{yxy}, \chi_{yyx}, \chi_{zxx}, \chi_{zzy}, \chi_{zzx}, \chi_{zxx}, \chi_{zxx}.$$

To consider the SHG wave in the sample coordinates (x', y', z), we decomposed the tangential components of the fundamental wave in the laboratory coordinates (x, y, z). The two coordinate systems can be transformed into each other according to the conventional rule of three-dimensional coordinate rotation that is described by two angles α and β , where (x, y, z) is first rotated around the y axis by α and then around the z axis by β to obtain (x', y', z). Therefore, the electric field components of the fundamental wave inside the thin film ($E_{x'}^{\omega}, E_{y'}^{\omega}, E_{z'}^{\omega}$) are:

$$E_{x'}^{\omega} = (E_x^{\omega} \cos \alpha + E_z^{\omega} \sin \alpha) \cos \beta - E_y^{\omega} \sin \beta$$

$$E_{y'}^{\omega} = (E_x^{\omega} \cos \alpha + E_z^{\omega} \sin \alpha) \sin \beta + E_y^{\omega} \cos \beta$$

$$E_{z'}^{\omega} = -E_x^{\omega} \sin \alpha + E_z^{\omega} \cos \alpha$$

Then, the electric field components of the SHG wave contributed by the electric dipole ($E_{x'}^{2\omega}, E_{y'}^{2\omega}, E_{z'}^{2\omega}$) are

$$E_{x'}^{2\omega} = (E_{x'}^{2\omega} \cos \beta + E_{y'}^{2\omega} \sin \beta) \cos \alpha - E_{z'}^{2\omega} \sin \alpha$$

$$E_{y'}^{2\omega} = E_{y'}^{2\omega} \cos \beta - E_{x'}^{2\omega} \sin \beta$$

$$E_{z'}^{2\omega} = (E_{x'}^{2\omega} \cos \beta + E_{y'}^{2\omega} \sin \beta) \sin \alpha + E_{z'}^{2\omega} \cos \alpha$$

The SHG of three equivalent monoclinic domains, the orientations of which in the laboratory coordinates are rotated by 120° around the z axis from each other, can then be obtained by coherently adding up the contribution of each domain: $I_{\text{total}}^{2\omega} = |E_{\theta}^{2\omega} + E_{\theta+120^\circ}^{2\omega} + E_{\theta+240^\circ}^{2\omega}|^2$.

For the electric quadrupole contribution of a centrosymmetric rhombohedral structure (point group $\bar{3}m$), the third-order susceptibility tensors are

$$\chi_{zzzz}, \chi_{xxxx} = \chi_{yyyy} = \chi_{xyyy} + \chi_{xyyx} + \chi_{xyxy},$$

$$\chi_{xxyy} = \chi_{yyxx}, \chi_{xyyx} = \chi_{yxxy}, \chi_{xyxy} = \chi_{yxyx},$$

$$\chi_{yyzz} = \chi_{xxzz}, \chi_{zzyy} = \chi_{zzxx}, \chi_{zyyz} = \chi_{zxxz}, \chi_{zyzy} = \chi_{xzzx},$$

$$\chi_{xxzx} = -\chi_{xyyz} = -\chi_{yxzy} = -\chi_{yyxz},$$

$$\chi_{xxzx} = -\chi_{xyyz} = -\chi_{yxzy} = -\chi_{yyxz},$$

$$\chi_{xxzx} = -\chi_{xzzy} = -\chi_{zyzy} = -\chi_{zyyx},$$

$$\chi_{xxzx} = -\chi_{zzyy} = -\chi_{zyzy} = -\chi_{zyyx},$$

$$\chi_{zyzy} = \chi_{xxzx}, \chi_{zyzy} = \chi_{xxzx}$$

The analytical expressions for SHG used for fitting are

$$I^{\text{PP}}(2\omega) = A_1 \left[(\chi_{zyzy} - 2\chi_{zzyy} + \chi_{zzzz} + \chi_{zyyy} \sin(3\phi))^2 + (2\chi_{xxyy} + \chi_{xyxy} - 2\chi_{xxxy} + \chi_{yzyz} + (\chi_{yyzy} - \chi_{yyyz}) \sin(3\phi))^2 \right]$$

$$I^{\text{PS}}(2\omega) = A_2 (\chi_{xyxy} - \chi_{yyzy} \sin(3\phi))^2 + (\chi_{zyzy} + \chi_{zzyy} \sin(3\phi))^2$$

$$I^{\text{SP}}(2\omega) = A_3 (\chi_{yyzy} - 2\chi_{yyyz}) \cos(3\phi)^2$$

$$I^{\text{SS}}(2\omega) = A_4 (\chi_{yyzy} \cos(3\phi))^2$$

STEM measurement and analyses

The cross-sectional STEM specimen was prepared by first thinning the sample using a focused ion beam milling workstation (Helios NanoLab 650, FEI Co) with low-energy ion beams (<2 kV), followed by focused low-energy (<500 eV) Ar-ion milling (NanoMill 1040, E.A. Fischione Instruments). Zone axis [110] was predetermined by high-resolution XRD.

Atomic-resolution ABF-STEM experiments were performed at room temperature using spherical aberration probe-corrected STEM with an acceleration voltage of 200 kV (JEM-ARM200F, JEOL Ltd). The instrument was equipped with a cold-field emission gun installed at the National Center for Inter-University Research Facilities, Seoul National University, South Korea. The TEM specimen was cleaned using an ion cleaner (JEC-4000DS, JEOL Ltd) before the STEM experiments. For STEM analyses, the semiconvergence angle was set to 24 mrad and the semicollection angle range was set to 12–24 mrad.

To minimize scan distortion and enhance the signal-to-noise ratio, 20 frames of serial STEM images were acquired with a short dwell time of 2 $\mu\text{s px}^{-1}$. Each image was 1,024 \times 1,024 in size. The image series was registered using both rigid and nonrigid methods, which yielded similar results⁴². The atomic positions were extracted using a two-dimensional Gaussian fitting method with seven parameters based on a customized MATLAB script. To eliminate the artefact induced by the tail of heavy elements, atomic positions were calculated in atomic mass order after removing the larger atomic peaks.

Low-temperature magnetism and transport measurements

Conventional photolithography and ion milling were used to pattern the SrRuO₃ films into the Hall bar geometry. The channel size was minimized to 50 \times 50 μm^2 . Pt (50 nm) electrodes were sputtered onto the Hall bar contacts to reduce contact resistance. Magnetization measurements were performed using a superconducting quantum interference device magnetometer (MPMS; Quantum Design). The longitudinal and transverse resistance were measured using a physical properties measurement system (Quantum Design) on standard Hall bars. Magnetic field angle-dependent Hall effect measurements were carried out with a homemade rotational stage.

Reporting summary

Further information on research design is available in the Nature Portfolio Reporting Summary linked to this article.

Data availability

Source data for the main figures are provided with this paper. These data are available at the figshare repository (<https://doi.org/10.6084/m9.figshare.22586689>). All other data related to this study are available from the corresponding authors on request.

References

33. Kresse, G. & Furthmüller, J. Efficient iterative schemes for ab initio total-energy calculations using a plane-wave basis set. *Phys. Rev. B* **54**, 11169 (1996).
34. Blöchl, P. E. Projector augmented-wave method. *Phys. Rev. B* **50**, 17953 (1994).
35. Liechtenstein, A. I., Anisimov, V. I. & Zaanen, J. Density-functional theory and strong interactions: orbital ordering in Mott–Hubbard insulators. *Phys. Rev. B* **52**, R5467 (1995).
36. Grånäs, O., Marco, I. D., Eriksson, O., Nordström, L. & Etz, C. Electronic structure, cohesive properties, and magnetism of SrRuO₃. *Phys. Rev. B* **90**, 165130 (2014).
37. Huang, A., Jeng, H.-T. & Chang, C.-H. First-principles calculations predict tunable large magnetic anisotropy due to spin-polarized quantum-well resonances in nanometer-thick SrRuO₃ films: implications for spintronic devices. *ACS Appl. Nano Mater.* **4**, 5932–5939 (2021).
38. Ryee, S. & Han, M. J. The effect of double counting, spin density, and Hund interaction in the different DFT+U functionals. *Sci. Rep.* **8**, 9559 (2018).
39. Dang, H. T. et al. Electronic correlations, magnetism, and Hund's rule coupling in the ruthenium perovskites SrRuO₃ and CaRuO₃. *Phys. Rev. B* **91**, 195149 (2015).
40. Li, G., Huang, X., Hu, J. & Zhang, W. Shear-strain gradient induced polarization reversal in ferroelectric BaTiO₃ thin films: a first-principles total energy study. *Phys. Rev. B* **95**, 144111 (2017).
41. Kim, S. H. et al. A compact and stable incidence-plane-rotating second harmonics detector. *Rev. Sci. Instrum.* **92**, 043905 (2021).
42. Savitzky, B. H. et al. Image registration of low signal-to-noise cryo-STEM data. *Ultramicroscopy* **191**, 56–65 (2018).

Acknowledgements

This work was supported by the Research Center Program of the Institute for Basic Science in Korea (IBS-R009-D1) and by the National Research Foundation of Korea (NRF) as funded by the Korean Ministry of Science and ICT (MSIT; Grant Nos. 2021R1A5A1032996, 2023R1A2C1007073, 2022R1A3B1077234 and 2022M3H4A1A04074153). The STEM measurements were supported by the National Center for Inter-University Research Facilities at Seoul National University. This work was supported by Samsung Electronics Co, Ltd (No. IO201211–08061-01). This paper is supported by the Basic Science Research Institute Fund (NRF Grant No. 2021R1A6A1A10042944). S.Y.P. was supported by the NRF as funded by MSIT (Grant No. 2021R1C1C1009494) and by the Basic Science Research Program through the NRF as funded by the

Ministry of Education (Grant Nos. 2021R1A6A1A03043957 and 2021R1A6A1A10044154). H.J. and J.S.L. were supported by MSIT (Grant No. 2022R1A2C2007847). Y.J.J. and T.H.K. acknowledge support from the Priority Research Centers Program through the NRF as funded by the Ministry of Education (Grant No. 2019R1A6A1A11053838). Experiments at PLS-II were supported in part by MSIT and the Pohang University of Science and Technology. L.W. is supported by the CAS Project for Young Scientists in Basic Research No. YSBR-084, the National Basic Research Program of China (Grant Nos. 2023YFA1406404 and 2020YFA0309100), the National Natural Science Foundation of China (Grant Nos. 12374094 and 12074365), and the USTC Center for Micro and Nanoscale Research and Fabrication for sample fabrications. The non-ambient XRD measurements were made using equipment housed within the X-ray Diffraction Research Technology Platform at the University of Warwick. D.W. acknowledges funding from the Engineering and Physical Sciences Research Council (Grant No. EP/V007688/1).

Author contributions

W.P., T.W.N. and D.L. conceived the idea and designed the experiments. W.P. grew the materials, fabricated the devices and performed the laboratory XRD, atomic force microscopy and magnetotransport measurements with help from E.K.K. D.W. assisted with the laboratory non-ambient XRD. S.Y.P. performed the first-principles calculations. C.J.R., H.J. and J.S.L. performed the SHG measurements. J.M., M.K., A.M.S. and S. Hindmarsh performed the STEM measurements. W.P., J.K., E.K.K., Y.J.J. and T.H.K. performed the synchrotron XRD. S. Hahn, L.S. and C.K. performed the band structure analysis. W.P., Z.L., J.Z. and L.W. performed the magnetization measurements. Y.J. contributed to the data analysis. W.P. and D.L. analysed the data and wrote the manuscript, with input from all authors. D.L. directed the overall research.

Competing interests

The authors declare no competing interests.

Additional information

Supplementary information The online version contains supplementary material available at <https://doi.org/10.1038/s41567-023-02333-8>.

Correspondence and requests for materials should be addressed to Wei Peng, Se Young Park, Tae Won Noh or Daesu Lee.

Peer review information *Nature Physics* thanks Gustau Catalan and the other, anonymous, reviewer(s) for their contribution to the peer review of this work.

Reprints and permissions information is available at www.nature.com/reprints.

Reporting Summary

Nature Portfolio wishes to improve the reproducibility of the work that we publish. This form provides structure for consistency and transparency in reporting. For further information on Nature Portfolio policies, see our [Editorial Policies](#) and the [Editorial Policy Checklist](#).

Statistics

For all statistical analyses, confirm that the following items are present in the figure legend, table legend, main text, or Methods section.

- | | |
|-------------------------------------|--|
| n/a | Confirmed |
| <input type="checkbox"/> | <input checked="" type="checkbox"/> The exact sample size (n) for each experimental group/condition, given as a discrete number and unit of measurement |
| <input checked="" type="checkbox"/> | <input type="checkbox"/> A statement on whether measurements were taken from distinct samples or whether the same sample was measured repeatedly |
| <input checked="" type="checkbox"/> | <input type="checkbox"/> The statistical test(s) used AND whether they are one- or two-sided
<i>Only common tests should be described solely by name; describe more complex techniques in the Methods section.</i> |
| <input checked="" type="checkbox"/> | <input type="checkbox"/> A description of all covariates tested |
| <input checked="" type="checkbox"/> | <input type="checkbox"/> A description of any assumptions or corrections, such as tests of normality and adjustment for multiple comparisons |
| <input type="checkbox"/> | <input checked="" type="checkbox"/> A full description of the statistical parameters including central tendency (e.g. means) or other basic estimates (e.g. regression coefficient) AND variation (e.g. standard deviation) or associated estimates of uncertainty (e.g. confidence intervals) |
| <input checked="" type="checkbox"/> | <input type="checkbox"/> For null hypothesis testing, the test statistic (e.g. F , t , r) with confidence intervals, effect sizes, degrees of freedom and P value noted
<i>Give P values as exact values whenever suitable.</i> |
| <input checked="" type="checkbox"/> | <input type="checkbox"/> For Bayesian analysis, information on the choice of priors and Markov chain Monte Carlo settings |
| <input checked="" type="checkbox"/> | <input type="checkbox"/> For hierarchical and complex designs, identification of the appropriate level for tests and full reporting of outcomes |
| <input checked="" type="checkbox"/> | <input type="checkbox"/> Estimates of effect sizes (e.g. Cohen's d , Pearson's r), indicating how they were calculated |

Our web collection on [statistics for biologists](#) contains articles on many of the points above.

Software and code

Policy information about [availability of computer code](#)

Data collection Vienna ab initio simulation package for first-principles density functional theory calculation

Data analysis MATLAB to analyze the SHG, STEM, and Hall effect measurement results

For manuscripts utilizing custom algorithms or software that are central to the research but not yet described in published literature, software must be made available to editors and reviewers. We strongly encourage code deposition in a community repository (e.g. GitHub). See the Nature Portfolio [guidelines for submitting code & software](#) for further information.

Data

Policy information about [availability of data](#)

All manuscripts must include a [data availability statement](#). This statement should provide the following information, where applicable:

- Accession codes, unique identifiers, or web links for publicly available datasets
- A description of any restrictions on data availability
- For clinical datasets or third party data, please ensure that the statement adheres to our [policy](#)

Source data for the main figures are provided with this paper. These data are available at the figshare repository (<https://doi.org/10.6084/m9.figshare.22586689>). All other data related to this study are available from the corresponding authors on request.

Research involving human participants, their data, or biological material

Policy information about studies with [human participants or human data](#). See also policy information about [sex, gender \(identity/presentation\), and sexual orientation](#) and [race, ethnicity and racism](#).

Reporting on sex and gender	Use the terms sex (biological attribute) and gender (shaped by social and cultural circumstances) carefully in order to avoid confusing both terms. Indicate if findings apply to only one sex or gender; describe whether sex and gender were considered in study design; whether sex and/or gender was determined based on self-reporting or assigned and methods used. Provide in the source data disaggregated sex and gender data, where this information has been collected, and if consent has been obtained for sharing of individual-level data; provide overall numbers in this Reporting Summary. Please state if this information has not been collected. Report sex- and gender-based analyses where performed; justify reasons for lack of sex- and gender-based analysis.
Reporting on race, ethnicity, or other socially relevant groupings	Please specify the socially constructed or socially relevant categorization variable(s) used in your manuscript and explain why they were used. Please note that such variables should not be used as proxies for other socially constructed/relevant variables (for example, race/ethnicity should not be used as a proxy for socioeconomic status). Provide clear definitions of the relevant terms used, how they were provided (by the participants/respondents, the researchers, or third parties), and the method(s) used to classify people into the different categories (e.g. self-report, census or administrative data, social media data, etc.) Please provide details about how you controlled for confounding variables in your analyses.
Population characteristics	Describe the covariate-relevant population characteristics of the human research participants (e.g. age, genotypic information, past and current diagnosis and treatment categories). If you filled out the behavioural & social sciences study design questions and have nothing to add here, write "See above."
Recruitment	Describe how participants were recruited. Outline any potential self-selection bias or other biases that may be present and how these are likely to impact results.
Ethics oversight	Identify the organization(s) that approved the study protocol.

Note that full information on the approval of the study protocol must also be provided in the manuscript.

Field-specific reporting

Please select the one below that is the best fit for your research. If you are not sure, read the appropriate sections before making your selection.

Life sciences Behavioural & social sciences Ecological, evolutionary & environmental sciences

For a reference copy of the document with all sections, see nature.com/documents/nr-reporting-summary-flat.pdf

Life sciences study design

All studies must disclose on these points even when the disclosure is negative.

Sample size	Describe how sample size was determined, detailing any statistical methods used to predetermine sample size OR if no sample-size calculation was performed, describe how sample sizes were chosen and provide a rationale for why these sample sizes are sufficient.
Data exclusions	Describe any data exclusions. If no data were excluded from the analyses, state so OR if data were excluded, describe the exclusions and the rationale behind them, indicating whether exclusion criteria were pre-established.
Replication	Describe the measures taken to verify the reproducibility of the experimental findings. If all attempts at replication were successful, confirm this OR if there are any findings that were not replicated or cannot be reproduced, note this and describe why.
Randomization	Describe how samples/organisms/participants were allocated into experimental groups. If allocation was not random, describe how covariates were controlled OR if this is not relevant to your study, explain why.
Blinding	Describe whether the investigators were blinded to group allocation during data collection and/or analysis. If blinding was not possible, describe why OR explain why blinding was not relevant to your study.

Behavioural & social sciences study design

All studies must disclose on these points even when the disclosure is negative.

Study description	Briefly describe the study type including whether data are quantitative, qualitative, or mixed methods (e.g. qualitative cross-sectional, quantitative experimental, mixed-methods case study).
Research sample	State the research sample (e.g. Harvard university undergraduates, villagers in rural India) and provide relevant demographic information (e.g. age, sex) and indicate whether the sample is representative. Provide a rationale for the study sample chosen. For studies involving existing datasets, please describe the dataset and source.

Sampling strategy	Describe the sampling procedure (e.g. random, snowball, stratified, convenience). Describe the statistical methods that were used to predetermine sample size OR if no sample-size calculation was performed, describe how sample sizes were chosen and provide a rationale for why these sample sizes are sufficient. For qualitative data, please indicate whether data saturation was considered, and what criteria were used to decide that no further sampling was needed.
Data collection	Provide details about the data collection procedure, including the instruments or devices used to record the data (e.g. pen and paper, computer, eye tracker, video or audio equipment) whether anyone was present besides the participant(s) and the researcher, and whether the researcher was blind to experimental condition and/or the study hypothesis during data collection.
Timing	Indicate the start and stop dates of data collection. If there is a gap between collection periods, state the dates for each sample cohort.
Data exclusions	If no data were excluded from the analyses, state so OR if data were excluded, provide the exact number of exclusions and the rationale behind them, indicating whether exclusion criteria were pre-established.
Non-participation	State how many participants dropped out/declined participation and the reason(s) given OR provide response rate OR state that no participants dropped out/declined participation.
Randomization	If participants were not allocated into experimental groups, state so OR describe how participants were allocated to groups, and if allocation was not random, describe how covariates were controlled.

Ecological, evolutionary & environmental sciences study design

All studies must disclose on these points even when the disclosure is negative.

Study description	Briefly describe the study. For quantitative data include treatment factors and interactions, design structure (e.g. factorial, nested, hierarchical), nature and number of experimental units and replicates.
Research sample	Describe the research sample (e.g. a group of tagged <i>Passer domesticus</i> , all <i>Stenocereus thurberi</i> within Organ Pipe Cactus National Monument), and provide a rationale for the sample choice. When relevant, describe the organism taxa, source, sex, age range and any manipulations. State what population the sample is meant to represent when applicable. For studies involving existing datasets, describe the data and its source.
Sampling strategy	Note the sampling procedure. Describe the statistical methods that were used to predetermine sample size OR if no sample-size calculation was performed, describe how sample sizes were chosen and provide a rationale for why these sample sizes are sufficient.
Data collection	Describe the data collection procedure, including who recorded the data and how.
Timing and spatial scale	Indicate the start and stop dates of data collection, noting the frequency and periodicity of sampling and providing a rationale for these choices. If there is a gap between collection periods, state the dates for each sample cohort. Specify the spatial scale from which the data are taken.
Data exclusions	If no data were excluded from the analyses, state so OR if data were excluded, describe the exclusions and the rationale behind them, indicating whether exclusion criteria were pre-established.
Reproducibility	Describe the measures taken to verify the reproducibility of experimental findings. For each experiment, note whether any attempts to repeat the experiment failed OR state that all attempts to repeat the experiment were successful.
Randomization	Describe how samples/organisms/participants were allocated into groups. If allocation was not random, describe how covariates were controlled. If this is not relevant to your study, explain why.
Blinding	Describe the extent of blinding used during data acquisition and analysis. If blinding was not possible, describe why OR explain why blinding was not relevant to your study.
Did the study involve field work?	<input type="checkbox"/> Yes <input type="checkbox"/> No

Field work, collection and transport

Field conditions	Describe the study conditions for field work, providing relevant parameters (e.g. temperature, rainfall).
Location	State the location of the sampling or experiment, providing relevant parameters (e.g. latitude and longitude, elevation, water depth).
Access & import/export	Describe the efforts you have made to access habitats and to collect and import/export your samples in a responsible manner and in compliance with local, national and international laws, noting any permits that were obtained (give the name of the issuing authority, the date of issue, and any identifying information).
Disturbance	Describe any disturbance caused by the study and how it was minimized.

Reporting for specific materials, systems and methods

We require information from authors about some types of materials, experimental systems and methods used in many studies. Here, indicate whether each material, system or method listed is relevant to your study. If you are not sure if a list item applies to your research, read the appropriate section before selecting a response.

Materials & experimental systems

- | n/a | Included in the study |
|-------------------------------------|--|
| <input checked="" type="checkbox"/> | <input type="checkbox"/> Antibodies |
| <input checked="" type="checkbox"/> | <input type="checkbox"/> Eukaryotic cell lines |
| <input checked="" type="checkbox"/> | <input type="checkbox"/> Palaeontology and archaeology |
| <input checked="" type="checkbox"/> | <input type="checkbox"/> Animals and other organisms |
| <input checked="" type="checkbox"/> | <input type="checkbox"/> Clinical data |
| <input checked="" type="checkbox"/> | <input type="checkbox"/> Dual use research of concern |
| <input checked="" type="checkbox"/> | <input type="checkbox"/> Plants |

Methods

- | n/a | Included in the study |
|-------------------------------------|---|
| <input checked="" type="checkbox"/> | <input type="checkbox"/> ChIP-seq |
| <input checked="" type="checkbox"/> | <input type="checkbox"/> Flow cytometry |
| <input checked="" type="checkbox"/> | <input type="checkbox"/> MRI-based neuroimaging |